IEEE Access
Multidisciplinary | Rapid Review | Open Access Journal

IEEE GEOSCIENCE AND REMOTE SENSING SOCIETY SECTION

Received 24 February 2025, accepted 5 March 2025, date of publication 10 March 2025, date of current version 19 March 2025.

Digital Object Identifier 10.1109/ACCESS.2025.3549443

RESEARCH ARTICLE

WGAN-GP-Based Conditional GAN (cGAN) With Extreme Critic for Precipitation Downscaling in a Key Agricultural Region of the Northeastern U.S.

JANGHO LEE[1] AND SUN YOUNG PARK[2]

[1]Department of Earth and Environmental Sciences, University of Illinois Chicago, Chicago, IL 60607, USA
[2]Department of Civil and Environmental Engineering, University of Illinois Urbana–Champaign, Champaign, IL 61820, USA

Corresponding author: Jangho Lee (jholee@uic.edu)

This work was supported by the U.S. Department of Energy, Office of Science, Office of Biological and Environmental Research's Urban Integrated Field Laboratories, CROCUS Project research activity, under Award DE-SC0023226.

ABSTRACT This study develops a conditional Generative Adversarial Network with a multi-head Critic (cGAN_ext), under a Wasserstein GAN with gradient penalty (WGAN-GP) framework, to downscale coarse-resolution meteorological data into high-resolution precipitation fields. The model's U-Net Generator combines large-scale atmospheric inputs—2 m temperature, total column water vapor, mean sea-level pressure, and downsampled precipitation—with a noise tensor, while the Critic enforces adversarial constraints and explicitly classifies extreme events. By focusing on rare high-intensity rainfall within the adversarial training loop, cGAN_ext captures crucial tail behavior that can be overlooked by conventional approaches. Experimental results reveal that cGAN_ext not only preserves fine-grained spatial details but also better represents heavy precipitation episodes, thereby improving essential metrics such as mean squared error, fractions skill scores for extremes, and temporal correlation. Visual analysis further confirms the model's ability to reproduce sharp precipitation fronts and narrow bands, underscoring the benefits of integrating an extreme-classification objective into a WGAN-GP cGAN pipeline. This enhanced downscaling method offers more accurate and coherent high-resolution precipitation maps, supporting informed decision-making in agricultural planning and water resource management.

INDEX TERMS Precipitation, radar, multi-radar multi-sensor, generative adversarial network (GAN), conditional GAN, Wasserstein GAN, deep learning, machine learning, ERA-5, downscaling, climate informatics.

I. INTRODUCTION

The frequency and intensity of extreme precipitation events are significant in multiple sectors of the society, including agriculture, infrastructure, and human health [1], [2], [3], [4]. Moreover, extreme precipitation is a key driver of natural disasters, including landslides, hailstorms, and flooding.

One of the most severely impacted sectors due to shifting precipitation patterns—whether through extreme rainfall or prolonged drought—is agriculture [5], [6], [7], [8]. Changes in precipitation not only threaten crop yields but also disrupt planting and harvesting cycles, degrade soil quality, and strain water resources [9], [10], [11]. These challenges have cascading effects on food security, rural livelihoods, and global supply chains, underscoring the critical need for adaptive strategies to ensure agricultural resilience in the face of climate change.

A key characteristic of precipitation is its tendency to occur over short durations and within localized areas. Despite its constrained spatial and temporal scope, such events can have far-reaching impacts due to the high variability of precipitation patterns. In regions where extreme rainfall alternates with periods of drought, the unpredictability of water availability exacerbates agricultural challenges. Farmers often bear the

The associate editor coordinating the review of this manuscript and approving it for publication was Andrea Rey.

burden of investing in water management infrastructure, such as drainage systems and flood barriers, to mitigate these risks [12], [13], [14], [15].

Given the sector's vulnerability, it is critical for climate models to accurately project and detect precipitation events to enable better risk mitigation and enhance preparedness. However, current climate models have notable limitations, particularly in terms of spatial and temporal resolution. For instance, widely used global climate models (GCMs) such as Community Earth System Model (CESM-2) [16], Max Planck Institute Grand Ensemble (MPI-GE) [17], or Canadian Earth System Model (CanESM) [18] typically have grid spacings of 30 to 80 km and temporal resolutions ranging from 1 to 24 hours. These scales are too coarse to accurately assess precipitation events, which often occur at finer spatial and temporal scales.

To address these limitations, efforts have been made to enhance the spatiotemporal resolution of climate model outputs using downscaling methods. These approaches generally fall into two main categories: dynamical downscaling and statistical downscaling. Dynamical downscaling employs high-resolution regional climate models (RCMs), such as the Weather Research and Forecasting (WRF) model, to simulate a smaller domain nested within a GCM. Dynamical downscaling has the advantage of preserving the physical consistency of weather variables, as it is based on the underlying physics of the atmosphere and interactions with land and ocean surfaces. However, it is computationally intensive, particularly when applied to large domains or when higher spatial and temporal resolutions are required.

In contrast, statistical downscaling relies on empirical relationships between large-scale climate variables from GCMs and local-scale climate observations. This approach is computationally efficient and capable of producing high-resolution outputs over extensive areas [19], [20], [21], [22]. However, its accuracy is heavily dependent on the availability and quality of observational data, as well as the robustness of the statistical relationships developed. Conventional statistical downscaling methods for precipitation include techniques such as multivariate analysis, mean-based methods, distribution-based methods, and machine-learning-based approaches.

Multivariate analysis considers multiple climate variables simultaneously to establish relationships between large-scale predictors and local precipitation, often using methods like principal component analysis (PCA) or canonical correlation analysis (CCA) to identify patterns and reduce dimensionality [23], [24]. Mean-based methods focus on adjusting large-scale climate outputs to match observed local means, typically using bias correction techniques, though they may struggle to accurately represent extremes or variability [25], [26]. Distribution-based methods model the statistical distribution of precipitation and adjust GCM outputs to better align with observed distributions, offering a more robust approach for capturing variability and extremes [27], [28]. Machine-learning-based methods, such as support vector machines (SVM) and random forests (RF), provide a modern alternative by capturing complex nonlinear relationships and interactions among predictors These methods have shown promise for precipitation modeling [19], [29], [30], [31].

More recently, neural network models, particularly deep learning approaches, have gained significant attention for their potential in downscaling precipitation data. Convolutional Neural Networks (CNNs) [32], [33], [34] and Long Short-Term Memory (LSTM) [35], [36] networks have demonstrated their ability to effectively capture the complex spatial and temporal characteristics of precipitation events. These models, however, are generally considered more basic forms of neural networks within the broader spectrum of deep learning techniques.

For more advanced techniques, Generative Adversarial Networks (GANs) have been gaining attention as a promising method for climate and weather downscaling [37], [38]. GANs operate through a generator-discriminator framework, where the generator creates high-resolution data from low-resolution inputs, and the discriminator evaluates the accuracy of the generated data against actual observations. This adversarial training process allows GANs to produce realistic, high-resolution precipitation data that effectively captures both the mean state and extremes, which are often challenging for traditional methods. One of the key strengths of GANs lies in their ability to learn complex, nonlinear relationships in the data without requiring explicit statistical assumptions. This makes them particularly suited for tasks like precipitation downscaling, where the spatial and temporal variability of rainfall can be highly complex. GANs have been shown to outperform conventional downscaling methods in capturing localized extreme events, such as intense rainfall or drought clusters.

Beyond basic GAN architectures, advanced variations such as Conditional GANs (cGANs) have been developed to incorporate auxiliary information, such as specific climate variables or spatial constraints, to further improve the fidelity of downscaled outputs [39], [40], [41]. These conditional approaches allow the models to generate precipitation patterns that are not only realistic but also physically consistent with the underlying atmospheric conditions.

The downside of traditional GAN methods is that they often suffer from mode collapse and training instability [42], [43], which can lead to poor diversity in generated samples and a lack of robustness in their outputs. To address these challenges, Wasserstein GAN based Gradient Penalty (WGAN-GP) approach have been employed [44], [45]. The WGAN-GP improves training stability by providing a more reliable measure of distance between the generated and real distributions, thereby mitigating mode collapse and ensuring better convergence. Furthermore, capturing extreme events is crucial in any precipitation downscaling approach. To address this, we explicitly equip our model with the capability to detect and better represent high-intensity rainfall, thereby

enhancing its performance on rare yet impactful precipitation extremes.

In this study, we aim to develop a WGAN-GP based cGAN model with extreme-detecting ability to downscale climate model-based reanalysis data to high spatial and temporal resolution, with a specific focus on the Corn Belt region of Illinois, USA. This region is highly sensitive to precipitation variability due to its reliance on agriculture, particularly corn and soybean production, which are vulnerable to both extreme rainfall and drought. By incorporating auxiliary information, such as temperature or sea level pressure patterns, into the cGAN framework, we aim to improve the resolution and detail of precipitation outputs while maintaining consistency with observed data patterns in the region.

The outcomes of this study are expected to provide useful tools for stakeholders in agriculture and water resource management. By generating high-resolution precipitation datasets, the WGAN-GP based cGAN model with extreme-detection ability will support better-informed decision-making, such as improving crop yield projections, optimizing water resource planning, and offering data-driven support for agricultural risk management strategies. This research contributes to the growing field of statistical climate downscaling by exploring the application of cGANs to enhance the precision of regional climate data and address challenges associated with coarse-resolution climate models.

II. DATA

A. STUDY REGION

Figure 1 illustrates the focus area of this study. The study centers on a region in Illinois, widely recognized as part of the Corn Belt due to its significant agricultural activity. The exact study area is highlighted in Figure 1b with a red box, covering approximately 150km × 150km. This region was selected for its agricultural importance, making it an ideal location for testing the proposed downscaling methods. Furthermore, the topography in this region is mostly flat, which minimizes the influence of complex terrain on precipitation patterns, allowing for a clearer evaluation of the model's performance in capturing localized precipitation dynamics.

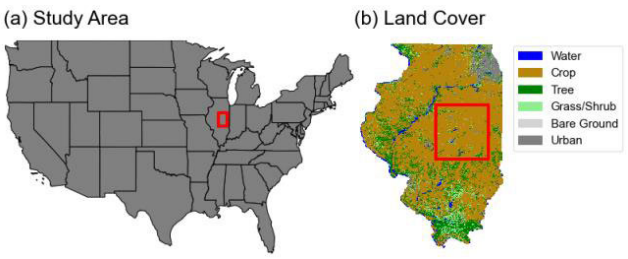

FIGURE 1. (a) Location of the study area (Illinois). (b) Major land cover in Illinois and the location of each NCEI stations used in this study.

B. MRMS PRECIPITATION DATA

The Multi-Radar/Multi-Sensor (MRMS) system [46] provides high-resolution precipitation data with exceptional spatial (1 km) and temporal (2 minutes) resolution. By integrating radar networks, surface and upper-air observations, lightning detection systems, satellite imagery, and forecast models, MRMS offers comprehensive and robust precipitation estimates across North America. Studies confirm its reliability in capturing spatial and temporal rainfall dynamics when validated against ground-based measurements and single radar systems [46], [47], [48], [49].

MRMS data serves as the high-resolution benchmark for this study's downscaling model. Its ability to resolve fine-scale rainfall features is critical for evaluating the performance of the cGAN model in reproducing localized extreme events, such as flash flooding and intense convective rainfall. These features are often underrepresented in coarse-resolution datasets like ERA-5.

While MRMS provides extensive spatial and temporal coverage, it has known limitations. Challenges include capturing precipitation in complex terrains where radar beam blockage or overshooting may occur and underestimating near-surface precipitation. These limitations are primarily observed in mountainous or densely urbanized regions [48], [49]. However, these concerns are minimal in the predominantly flat study region, where MRMS data is well-suited to capture precipitation dynamics accurately.

To align with the spatial resolution of ERA-5 (0.25°), MRMS data was systematically downsampled, creating a precipitation rate (PR) dataset. This PR dataset serves as a proxy for low-resolution climate model outputs while retaining sufficient detail for evaluating downscaling accuracy. The analysis period spans the wettest months (June–August) from 2018 to 2023, capturing high-impact precipitation events critical for agriculture in the study region.

By leveraging MRMS data, the proposed model not only achieves high spatial and temporal fidelity but also supports better-informed water resource planning and agricultural risk management. Previous studies [39], [50] demonstrate the efficacy of using MRMS-derived data in precipitation downscaling, reinforcing its pivotal role in this research.

C. ERA-5 REANALYSIS DATA

The lower-resolution dataset used in this study is the ERA-5 reanalysis dataset, which features a spatial resolution of 0.25° × 0.25° (consistent with PR data) and an hourly temporal resolution. Reanalysis data is produced by assimilating observations from various sources, such as satellites, weather stations, and radiosondes, into a numerical weather prediction (NWP) model to create a consistent, gridded dataset that represents past atmospheric conditions. This process blends observations with the physical principles encoded in the model, allowing for global coverage and the generation of variables that may not be directly observed.

Reanalysis datasets, such as ERA-5, are often used as proxies GCMs because they provide comprehensive and continuous data that reflect both observed and modeled atmospheric dynamics. While not explicitly a GCM, ERA-5's integration of observational data and model outputs enables it to act as a surrogate for GCMs, especially when studying historical climate conditions. Its lower resolution aligns well with that of many GCMs, making it a suitable candidate for use in downscaling applications that aim to bridge the gap between coarse climate model outputs and finer observational datasets.

In this study, we use 2-meter air temperature (T2M), total column water vapor (TCWV), and mean sea level pressure (MSL) as the coarse-resolution input variables. These variables were chosen based on their established relevance in prior downscaling studies [51], [52]. While incorporating additional variables, such as those at different pressure levels (e.g., 850 hPa), could improve model performance, we limit our selection to these three variables to balance accuracy with computational efficiency. To ensure temporal alignment with the PR data derived from MRMS, we interpolate the ERA-5 variables to a 20-minute resolution. Spatially, no further adjustments are needed, as the PR data, being a downsampled product, is designed to align with the spatial resolution of the ERA-5 dataset.

An example of the dataset used in this study is illustrated in Figure 2, where we present the MRMS, PR, T2M, TCWV, and MSL data for June 4, 2020, at 05:40. This figure highlights the differences in resolution between the input data and the desired output (downscaled) data, providing a clear depiction of the downscaling process and its objectives.

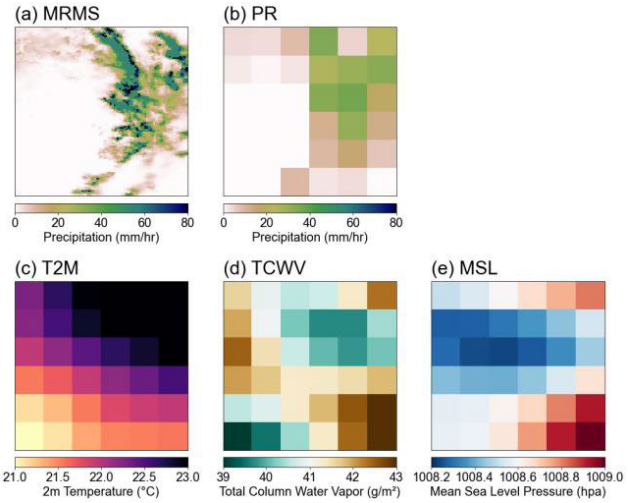

FIGURE 2. (a) MRMS precipitation pattern for the June 4, 2020, at 05:40. (b) Same as (a), but for downsampled MRMS (PR). (c-e) Same as (a), but for ERA-5 2m temperature (T2M), total column water vapor (TCWV), and mean sea level pressure (MSL), respectively.

D. MODEL SETUP

In this study, we aim to develop a regression model that takes PR and ERA-5-based variables—PR, T2M, TCWV and MSL—as inputs and produces MRMS as output. This approach can be viewed as enhancing the coarse-resolution dataset to match the higher-resolution precipitation data provided by MRMS. For training and testing, we temporally split the dataset. The five years of data from 2018 to 2022 are used as the training set, while data from 2023 is reserved for testing. The training set consists of a total of 33,120 timesteps (5 years $\times$ 92 days $\times$ 24 hours $\times$ 3 timesteps per hour), each represented as a 150 $\times$ 150 grid image. The testing set, with data from 2023, includes 6,624 timesteps with the same spatial resolution. This temporal split ensures that the model is evaluated on entirely unseen data, enabling a robust assessment of its generalization capabilities.

III. METHOD OF ANALYSIS

A. WGAN-GP-BASED CGAN WITH EXTREME CRITIC

1) GENERATIVE ADVERSARIAL NETWORKS (GANS)

A Generative Adversarial Network (GAN) [53], [54] are a class of deep learning models designed to learn data distributions by placing two networks in opposition. One of these networks is the Generator (G), which maps a random noise vector z to synthetic data $\hat{x}$. The other network is the Discriminator (D), or Critic in certain variants, which receives either real data x from the training set or generated data $\hat{x}$ from the Generator, then outputs a measure of how ''real'' or ''fake'' it believes each sample to be.

This setup is designed to include an adversarial training process, often described as a min-max game. In its classical form, the Generator attempts to minimize the Discriminator's ability to distinguish real from fake, whereas the Discriminator tries to maximize that same ability. Let P_{data} denote the real data distribution and let P_z denote the noise distribution from which z is drawn. The original GAN objective can be written (in simplified notation) as:

$$\min_G \max_D \left(E_{x\sim p_{data}}\left[\log D\left(x\right)\right] + E_{z\sim p_z}\left[\log\left(1 - D\left(G\left(z\right)\right)\right)\right]\right) \tag{1}$$

Here, $x \sim p_{data}$ represent the real data distribution (e.g., MRMS) and $z \sim p_z$ is a noise distribution. The term $E_{x\sim p_{data}}\left[\log D\left(x\right)\right]$ represents the expected log-probability that the Discriminator assigns to correctly identifying the real data, while $E_{z\sim p_z}\left[\log\left(1 - D\left(G\left(z\right)\right)\right)\right]$ measures the expected log-probability that the Discriminator correctly identifies the generated outputs $G\left(z\right)$ as fake.

2) CONDITIONAL GANS (CGAN)

A standard GAN only learns to map from noise z to synthetic data, ignoring any external context that might shape the distribution. Many real-world tasks, especially in meteorology, this process can involve strong dependencies on known variables. A conditional GAN (cGAN) incorporates additional inputs, referred to as the condition (x_{cond}) In this study, these inputs

include large-scale fields, including PR, T2M, TCWV, and MSL.

By feeding both z and x_{cond} into the Generator, the model learns to produce synthetic precipitation $\hat{x}$, that is consistent with the given atmospheric drivers. Simultaneously, the Discriminator (or Critic) also sees the same condition x_{cond} concatenated with either real or generated precipitation, thereby enforcing coherence between the two. This setup ensures that outputs from the Generator respect the large-scale physical states on which local precipitation depends.

3) WASSERSTEIN GAN WITH GRADIENT PENALTY (WGAN-GP)

Although cGANs guide the model to respect external conditions, classical GAN training can be unstable and prone to mode collapse, where the Generator produces only a narrow subset of possible precipitation patterns. Wasserstein GAN (WGAN) addresses these issues by adopting the Wasserstein distance (also called Earth Mover's distance) as a measure of divergence between real and generated distributions. Instead of classifying samples as real or fake, the Discriminator becomes a Critic that outputs a real number for each sample, indicating its "realness."

The WGAN-GP variant ensures that the Critic remains a Lipschitz function through a gradient penalty. The term "Lipschitz" means that the Critic's output cannot change arbitrarily fast with respect to small changes in input, which stabilizes the training. To achieve this, WGAN-GP adds a penalty term to the Critic's objective that discourages large gradients. The Critic's full objective can be represented in simplified form as:

$$L_{Critic\_WGAN} = \left(E\left[D\left(x_{fake}\right)\right] - E\left[D\left(x_{real}\right)\right]\right) + \lambda E_{\hat{x}}\left[\left\|\nabla_{\hat{x}} D\left(\hat{x}\right)\right\|_2 - 1\right]^2 \quad (2)$$

In this equation, x_{fake} and x_{real} each denote the generated (fake) and existing (real) input data. The expression $\nabla_{\hat{x}} D\left(\hat{x}\right)$ denote the gradient of the critic D, with respect to $\hat{x}$. The notation $\left\|\nabla_{\hat{x}} D\left(\hat{x}\right)\right\|_2$ represents the L2 norm of the gradient, and this is further scaled by the factor λ. For the Generator in the WGAN-GP, the objective becomes:

$$L_{Generator\_WGAN} = -E\left[D\left(x_{fake}\right)\right] \quad (3)$$

This means that the Generator tries to maximize the Critic's score on the fake samples it produces. This process naturally leads the Generator to generate outputs that the Critic perceives as more "real," typically yielding more stable training than classical GANs.

4) MULTI-HEAD CRITIC FOR EXTREME PRECIPITATION

In precipitation downscaling, capturing the rare but impactful high-intensity events ($\geq$ 20 mm/hr precipitation, equivalent to 95th percentile) is crucial. Simply relying on a single scalar Critic output can lead to underrepresentation of these heavy tails, because the adversarial training often prioritizes matching the overall distribution rather than these rare extremes. By augmenting the Critic with an extreme classifier head, the model can focus on distinguishing extreme events directly, rather than hoping the generator captures these high values incidentally. Furthermore, model can provide gradient signals specific to rare but physically important samples.

To address this, we first label each scene of precipitation of extreme/non-extreme as if it contains at least one pixel of 20mm/hr precipitation. Based on this, we introduce another critic loss function called the Extreme Classification Loss function, inspired by the cross-entropy function. Mathematically, it can be expressed as:

$$L_{Extreme} = -\frac{1}{m}\sum_{i=1}^{m} \times \left[y_i \log\left(\sigma\left(D_c\left(x_i\right)\right)\right) + \left(1 - y_i \log\left(1 - \sigma\left(D_c\left(x_i\right)\right)\right)\right)\right] \quad (4)$$

where $D_c\left(x_i\right)$ is the Critic's classification head output for sample i, and $\sigma()$ is the sigmoid function so the classification logit $D_c\left(x_i\right)$ fit into the probability distribution between 0 and 1. Combining this with the L_{Critic_WGAN}, the total Loss function becomes:

$$L = L_{Critic\_WGAN} + \alpha L_{Extreme} \quad (5)$$

where α is a weighting factor. We have tested multiple α for this model, and $\alpha = 0.1$ was selected for the best performing model. By integrating this multi-head Critic into a WGAN-GP framework, our model explicitly focuses on both overall distribution alignment and the correct generation of extreme events—leading to more robust downscaling performance, especially in the upper tail of the precipitation distribution.

5) MODEL ARCHITECTURE

In this study, we use a conditional WGAN-GP design to transform coarse-resolution meteorological fields into fine-resolution precipitation maps (150×150). The generator follows a U-Net architecture, where four meteorological variables are concatenated along with a two-dimensional noise tensor (latent_dim = 2) across the channel dimension. This U-Net has five downsampling stages, each applying a pair of convolution and ReLU operations plus a max-pooling layer, resulting in progressively smaller spatial dimensions but richer feature channels (up to 1024 in the final downsampling). We then double this to 2048 channels in a bottleneck layer to capture broad-scale atmospheric context. On the upsampling side, a series of transposed convolutions restore the resolution step by step, and skip connections reintegrate feature maps from earlier layers to preserve small-scale precipitation details. Before returning the final precipitation field, an interpolation stage resizes the output to 150×150, ensuring spatial consistency.

The critic is designed as a multi-head network, taking five total channels—four meteorological fields plus one precipitation channel—and producing two logits to classify each sample as extreme or non-extreme, based on whether its maximum precipitation exceeds a threshold (extreme_threshold = 20.0). Real samples derive their label from the observed precipitation, while generated samples inherit the real sample's label. In addition to this classification head, the critic enforces the WGAN-GP objective by measuring how "real" or "fake" each precipitation field appears, stabilized via gradient penalties to maintain Lipschitz continuity and avoid training instabilities like mode collapse.

We train the network for epochs = 200, using batches of size batch_size = 128. We apply the Adam optimizer at learning_rate = 1e-4 and enable an early-stopping mechanism with patience = 25 epochs based on a validation mean squared error (MSE) criterion. Each epoch proceeds with the critic update first: we generate a batch of synthetic precipitation using a detached generator output—so it does not propagate gradients back to the generator—and compute a binary cross-entropy loss on the critic's extreme classification head. We also maintain the WGAN-GP aspect by having the critic differentiate between real and fake inputs. Next, we perform a fresh pass of the generator to update its parameters with a combined loss that includes an MSE term (comparing generated and real precipitation) plus an extreme classification penalty weighted by alpha_class_loss = 0.1. This separate classification term encourages the generator to produce rare high-intensity rainfall when conditions warrant it. If the validation MSE improves, we save the best generator parameters.

At inference time, we load the trained models, concatenate new coarse-scale fields with a random noise tensor and pass this through the generator to obtain high-resolution precipitation predictions. Because each sample retains the same resolution (150 × 150) as the training outputs, operational or climate analysts can directly evaluate these forecasts in downstream applications. Overall, this integrated setup—pairing a U-Net generator with a multi-head WGAN-GP critic—balances spatial accuracy, temporal realism, and explicit focus on extreme precipitation events, addressing a key shortcoming in conventional deep learning downscaling approaches. The schematic of the model structure can be found in Figure 3.

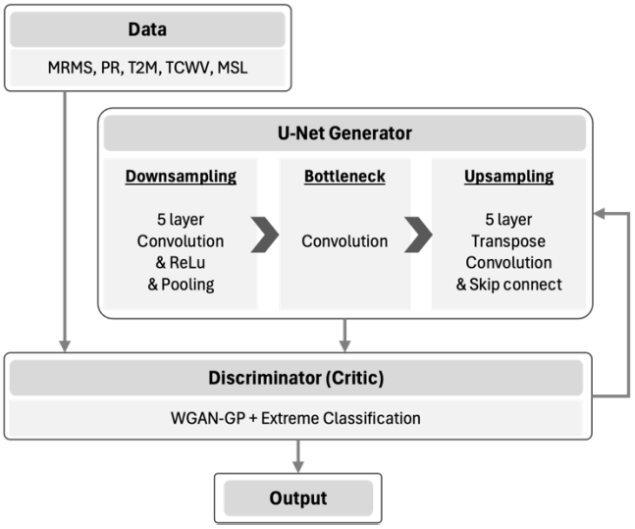

FIGURE 3. Simplified schematic of cGAN_ext architecture used in this study.

B. EFFICIENT SUB-PIXEL CONVOLUTIONAL NETWORK (ESPCN)

As a baseline model for comparison, we adopt the Efficient Sub-Pixel Convolutional Network (ESPCN) [55], [56], [57] which directly learns to rearrange low-resolution feature maps into high-resolution outputs through a sub-pixel (pixel-shuffle) operation. Unlike classical upsampling methods (e.g., bilinear interpolation or standard deconvolution), ESPCN simultaneously exploits learned convolutions and sub-pixel rearrangement to preserve fine-grained details.

The network first applies a series of convolutional layers to the coarse-scale meteorological inputs, extracting richer features at the native low resolution. Each convolution is followed by a ReLU activation. Subsequently, the sub-pixel convolution step (Pixel Shuffle) expands the spatial resolution. Specifically, the final convolution layer produces $r^2 \times C_{out}$ channels, where r is the scale factor (set to 2 in our experiments) and $C_{out} = 1$ for the precipitation output channel. This output is then reshaped by Pixel Shuffle into a (C_{out}, rH, rW) tensor, effectively super-resolving the precipitation field from low to high resolution.

In our configuration, we use three convolutional layers: a 5 × 5 filter in the first layer, followed by a 3 × 3 filter, and ending with the sub-pixel convolution layer that outputs $r^2 = 4$ channels. We train the model with a pixel-wise MSE loss and the Adam optimizer. During training, batches of coarse-scale meteorological inputs are fed into ESPCN, whose outputs are directly compared against the target high-resolution precipitation. Once trained, the network can be applied to any new coarse-scale input to generate high-resolution precipitation predictions in real time.

C. EVALUATION METRICS

1) GENERAL METRIC

Here we introduce some evaluation metrics that can be used to compare the performance of cGAN_ext, cGAN and ESPCN. First, we use a Kling-Gupta Efficiency (KGE) for general performance evaluation. KGE is defined as:

$$KGE = 1 - \sqrt{(r-1)^2 + \left(\frac{\sigma_{model}}{\sigma_{mrms}}\right)^2 + \left(\frac{\mu_{model}}{\mu_{mrms}}\right)^2} \quad (6)$$

where r is the Pearson correlation coefficient between MRMS and the model, while σ and μ each represents the standard deviation and mean of the dataset. A perfect prediction will yield KGE value of 1.

2) SPATIAL METRIC

For the spatial performance metric, we compute the Structural Similarity Index (SSI), which measures the similarity between two fields by comparing their luminance, contrast, and structure. The components of SSI are defined as:

$$l(x,y) = \frac{2\mu_x\mu_y + C_1}{\mu_x^2 + \mu_y^2 + C_1} \tag{7}$$

$$c(x,y) = \frac{2\sigma_x\sigma_y + C_2}{\sigma_x^2 + \mu\sigma_y^2 + C_2} \tag{8}$$

$$s(x,y) = \frac{\sigma_{xy} + C_3}{\sigma_x\sigma_y + C_3} \tag{9}$$

where Equations 5, 6, and 7 each represents Luminance, Contrast, and Structure. μ_x and μ_y depicts the mean values of the two fields, σ_x and σ_y represents the standard deviations, and σ_{xy} represents the covariance. C_1, C_2, and C_3 are constants to stabilize the division (for cases where mean or standard values are close to zero) and is set to 0.01 for C_1 and C_2, 0.005 for C_3. The final SSI overall combines these three components by:

$$SSI(x,y) = l(x,y) \times c(x,y) \times s(x,y) \tag{10}$$

SSI can range from 0 to 1, where the value close to 1 represents more similarity.

3) EXTREME METRIC

Lastly, we evaluate the models based on the extreme events. To evaluate this, we use the Fractions Skill Score (FSS). Traditional metrics such as MSE often penalize model predictions heavily for small spatial displacements, even when the model accurately captures general precipitation patterns. FSS addresses this limitation by considering spatial neighborhoods, making it particularly effective for assessing extreme cases. For this analysis, we focus on extreme precipitation events with a threshold of 7.5 mm/hr. The first step is to threshold the data based on this heavy precipitation case. Next, we calculate the neighborhood fractions. For each grid point (i, j), we compute the fraction of grid points within a surrounding 5 km neighborhood that exceed the threshold, denoted as $f(i, j)$, The FSS is then calculated using the formula:

$$FSS = 1 - \frac{\sum_{i,j}(f_{pred}(i,j) - f_{obs}(i,j)}{\sum_{i,j}\left(f_{pred}(i,j)^2 + f_{obs}(i,j)^2\right)} \tag{11}$$

FSS values range from 0 to 1, where a value close to 1 indicates a perfect model prediction.

Additionally, we classify each scene as "extreme" or "non-extreme" by examining its maximum precipitation pixel. Specifically, we use a threshold of 20 mm/hr—corresponding to the 95th percentile of the maximum precipitation across all samples. Any scene whose maximum pixel meets or exceeds this threshold is labeled "extreme," and all others are considered "non-extreme." Based on these labels, we then compute precision, recall, and the F1 score as follows:

$$Precision = \frac{True\ Positive}{True\ Positive + False\ Positive} \tag{12}$$

$$Recall = \frac{True\ Positive}{True\ Positive + False\ Negative} \tag{13}$$

$$F1 = \frac{2 \times Precision \times Recall}{Precision + Recall} \tag{14}$$

IV. RESULTS

A. METRIC-BASED EVALUATION

We compare the performance of three models—cGAN_ext, cGAN, and ESPCN—using multiple metrics, as summarized in Table 1. In terms of mean squared error (MSE), cGAN_ext achieves the lowest value (2.10), closely followed by cGAN (2.12), while ESPCN is noticeably higher at 2.54. This indicates that both cGAN_ext and cGAN provide a closer overall fit to the observed data compared to ESPCN.

To assess temporal dynamics, we compute the temporal correlation coefficient (TCC) for the area-averaged time series of precipitation. Both cGAN_ext and cGAN reach 0.99, reflecting their strong capability to capture rapid, real-world fluctuations, whereas ESPCN stands at 0.98. Despite the small numerical difference, these high correlations underscore that the adversarial training in cGAN_ext and cGAN helps preserve short-term variability more effectively than ESPCN's purely convolution-based approach.

In evaluating overall hydrological fidelity via the Kling-Gupta Efficiency (KGE), cGAN_ext again leads with 0.58, followed by cGAN at 0.56, and ESPCN at 0.40. This gap confirms that incorporating adversarial objectives—particularly the multi-head extension in cGAN_ext—further strengthens the consistency between model outputs and the observed precipitation distribution. We also measure the Structural Similarity Index (SSI) to gauge spatial quality, where both cGAN_ext and cGAN attain 0.93, while ESPCN trails at 0.78, suggesting that the U-Net-based adversarial methods capture fine spatial details more effectively.

For extreme events, a threshold-based Fractions Skill Score (FSS) indicates that cGAN_ext attains 0.87, marginally surpassing cGAN at 0.85 and ESPCN at 0.84. Moreover, although the Precision for extreme classification is perfect (1.0) across all three models, the Recall varies substantially: cGAN_ext improves recall to 0.23 over cGAN's 0.21, while ESPCN lags at 0.13. Consequently, cGAN_ext achieves the highest F1 score (0.38), cGAN the second-highest (0.35), and ESPCN the lowest (0.24). This pattern confirms that cGAN_ext's multi-head Critic helps capture rare but high-intensity precipitation events more reliably than the other approaches.

Overall, cGAN_ext consistently outperforms or closely matches cGAN in every metric, with ESPCN generally showing lower scores. By integrating a specialized extreme-event classification head, cGAN_ext demonstrates improved accuracy in both bulk statistics and tail events, making it a strong candidate for operational precipitation downscaling. The metrics used in this comparison are presented in Table 1.

TABLE 1. Evaluation metrics for cGAN_ext, cGAN and ESPCN.

Metric	cGAN_ext	cGAN	ESPCN
Mean Squared Error	2.10	2.12	2.54
Temporal Correlation Coefficient	0.99	0.99	0.98
Kling-Gupta Efficiency (KGE)	0.58	0.56	0.41
Structural Similarity Index (SSI)	0.93	0.93	0.78
Fractions Skill Score (FSS)	0.87	0.85	0.84
F1 Score	0.38	0.35	0.24

B. VISUAL CASE EVALUATION

We evaluate selected test cases visually to illustrate the comparative performance of cGAN_ext and ESPCN. We focus on three timesteps: June 29, 2023, at 18:40; July 5, 2023, at 21:40; and July 8, 2023, at 07:00. Each timestamp exhibits high precipitation rates and distinct evolving patterns. To capture temporal dynamics, we show a two-hour window around each time and compare results to the ground truth.

Figures 4 through 6 display precipitation fields for each selected period. The first column is MRMS (true precipitation), followed by the downsampled MRMS (model input) in the second column. The third and fourth columns depict the outputs from cGAN_ext and ESPCN, respectively.

From visual inspection, cGAN_ext generally replicates the MRMS patterns more closely than ESPCN. In Figure 4, a west-to-east precipitation front appears; cGAN_ext better preserves the front's width and structure. Similarly, in Figure 5, the narrow branch of precipitation that emerges after 21:40 is more clearly captured by cGAN_ext, whereas ESPCN underestimates the intensity and extent of this feature. In Figure 6, the Y-shaped precipitation structure between 06:40 and 07:20 stands out more distinctly in cGAN_ext, highlighting its ability to track fine-scale patterns and sharp transitions.

These qualitative gains stem from the adversarial training inherent in cGAN_ext. While ESPCN relies on a pixel-wise objective for upscaling, cGAN_ext's Critic drives the Generator to produce more realistic precipitation fields, capturing narrow bands and evolving structures that match the true data distribution more closely. This advantage is especially visible in complex precipitation systems requiring the preservation of both global configuration and localized details.

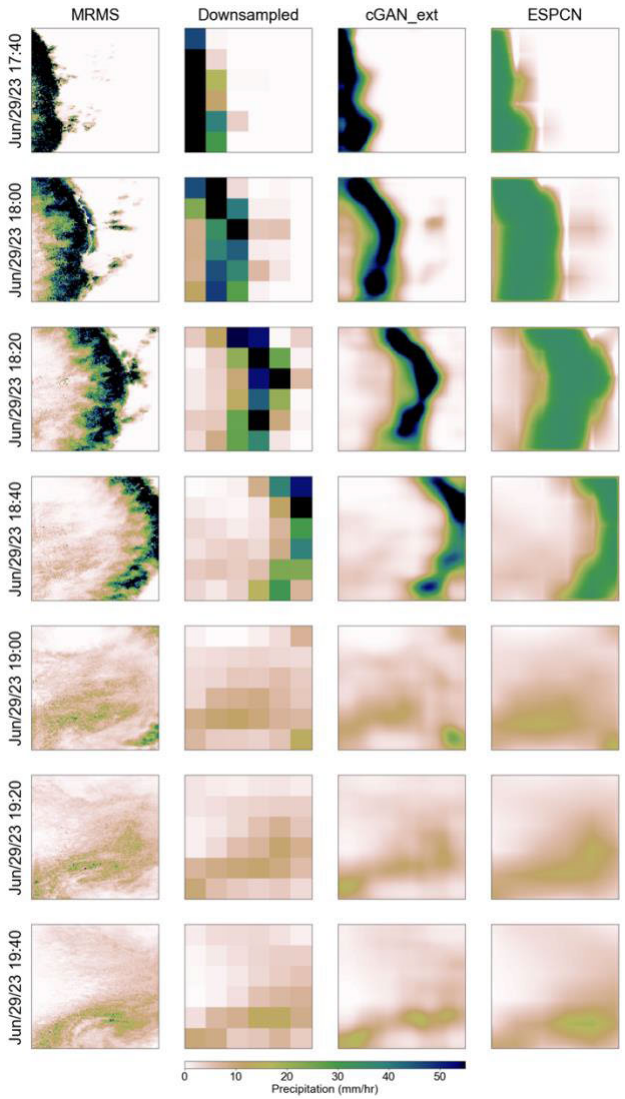

FIGURE 4. Precipitation patterns derived from MRMS (first column), downsampled MRMS (PR; second column), cGAN_ext estimations (third column), and ESPCN estimations (fourth column). The case begins on June 29, 2023, at 17:40 (first row) and is displayed at 20-minute intervals.

V. SUMMARY AND DISCUSSIONS

A. SUMMARY

This study introduced three models—cGAN_ext, cGAN, and ESPCN—for downscaling coarse-resolution meteorological data into fine-resolution precipitation fields. In cGAN_ext and cGAN, we leverage a conditional Generative Adversarial Network framework under the Wasserstein GAN with gradient penalty (WGAN-GP), where a U-Net Generator learns to reconstruct high-resolution precipitation from atmospheric variables such as T2M, MSL, TCWV, and downsampled precipitation inputs (PR), concatenated with a noise tensor. This U-Net design preserves both large-scale features and small-scale rainfall structures through a Bottleneck and skip connections, while the WGAN-GP Critic stabilizes adversarial training by applying gradient penalties.

We evaluated cGAN_ext, cGAN, and ESPCN across multiple metrics, including mean squared error (MSE), temporal correlation, Kling-Gupta Efficiency (KGE), structural similarity (SSI), fractions skill score (FSS) for extremes, and precision–recall statistics for identifying high-intensity events. Both cGAN variants outperformed ESPCN in capturing fine-scale precipitation details, with cGAN_ext slightly surpassing standard cGAN in terms of heavy rainfall representation. Visual inspections of challenging precipitation events confirmed that cGAN_ext and cGAN generate sharper rainfall fronts, narrower bands, and more realistic local structures than the purely convolution-based ESPCN. Overall, the WGAN-GP framework enabled stable training and

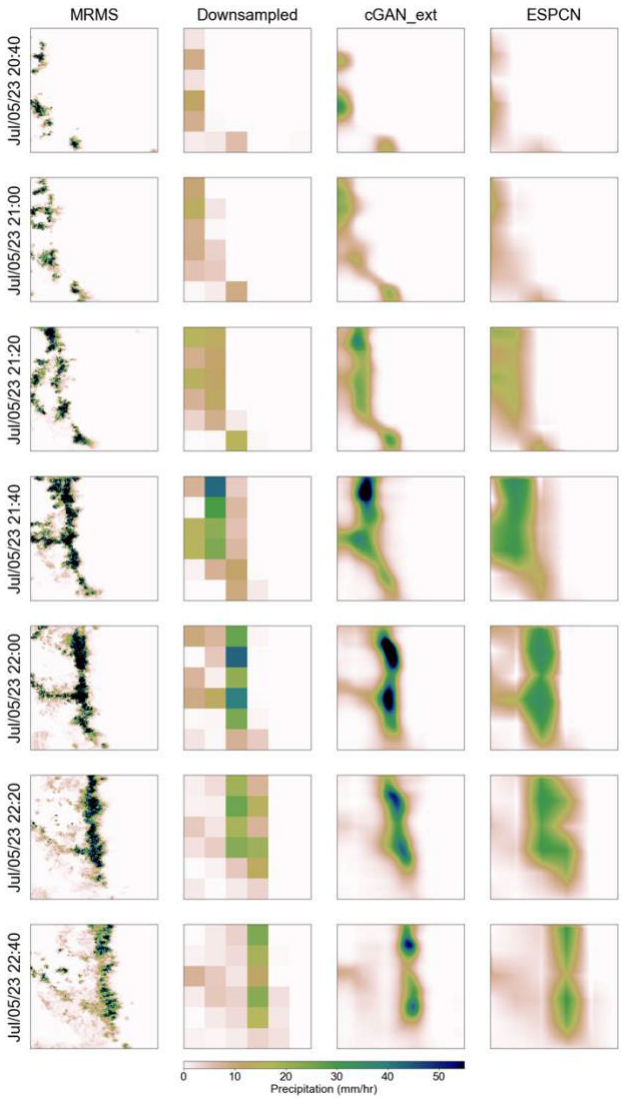

FIGURE 5. Same as Figure 4, but for the case on July 5, 2023, at 20:40.

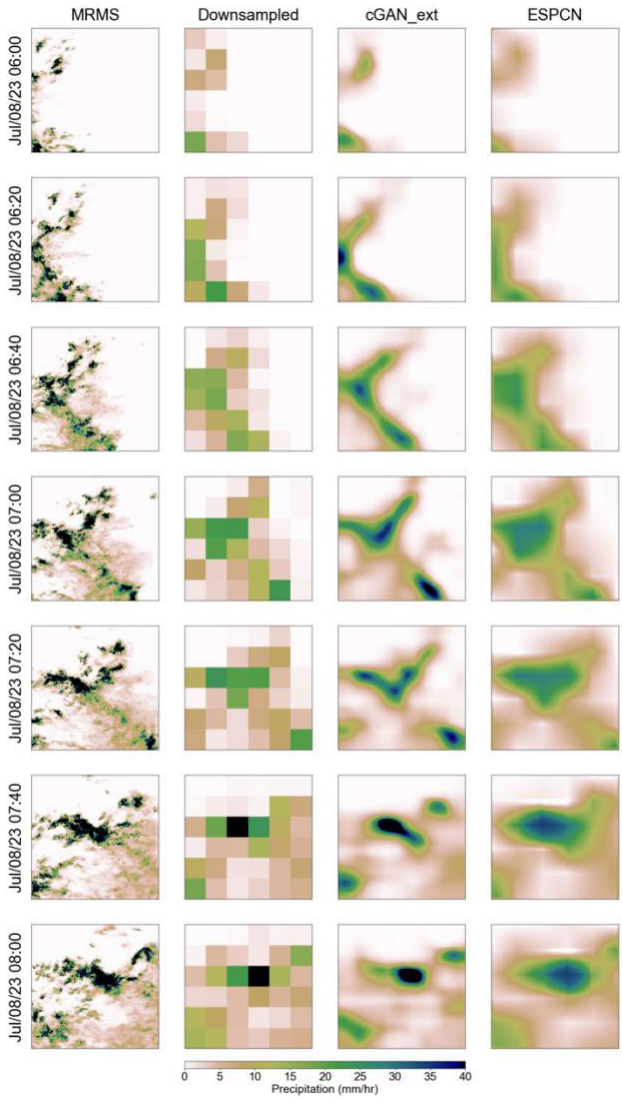

FIGURE 6. Same as Figure 4, but for the case on July 8, 2023, at 06:00.

robust spatiotemporal fidelity, especially for extremes, which are typically the most impactful yet difficult aspect of downscaling.

B. MODEL DISCUSSION

The key distinction among the three models lies in how they handle realism and rare events. ESPCN, as a baseline super-resolution CNN, learns upsampling via pixel-shuffling but relies purely on pixel-wise losses. While it reconstructs precipitation fields fairly well, it tends to smooth out extreme rainfall. By contrast, cGAN's adversarial training pushes the Generator to fit the observed precipitation distribution more closely, capturing localized intensity gradients and sharper transitions. Building on cGAN, cGAN_ext introduces an additional extreme-classification output in its Critic, encouraging the Generator to produce high-intensity precipitation where real observations exceed a threshold. This multi-head Critic mechanism provides a direct incentive for reproducing rare but critical tail events, yielding modest yet meaningful improvements over cGAN in metrics tied to extremes.

C. IMPLICATIONS

Several implications arise from this work. First, demonstrating that cGAN_ext (and to a slightly lesser extent, cGAN) excels at modeling high-intensity rainfall highlights its potential utility in operational contexts—such as flash flood forecasting or agricultural planning—where accurate depiction of extremes is vital. Second, the explicit conditioning on multiple meteorological variables ensures that the downscaled fields remain consistent with broader atmospheric states, an essential requirement for hydrological or agronomic modeling chains. Third, leveraging WGAN-GP addresses common stability issues in GAN training, providing a path toward more robust deep learning–based downscaling frameworks. Finally, because real-world weather systems vary in complexity, this methodology can be adapted

to incorporate additional atmospheric drivers or ensemble strategies, enhancing its applicability to diverse climates and future change scenarios.

D. LIMITATIONS AND FUTURE DIRECTIONS

While the cGAN_ext showed clear advantages, there are a few limitations that merit attention. First, the study region featured relatively modest topographical complexity, allowing precipitation to be driven largely by synoptic- or meso-scale forcings rather than orographic effects. More complex terrains could require additional atmospheric variables—like wind fields at multiple pressure levels—to capture the interplay of moist flow and orography. Furthermore, as with many data-driven deep learning approaches, regions or periods lacking extensive observations may challenge the network's ability to generalize. Robust data assimilation or transfer learning strategies could help bridge such gaps.

Another point of extension involves ensemble downscaling, in which multiple plausible realizations of precipitation fields are generated for a given condition. Such an approach would better represent inherent uncertainties, especially under future or extreme climate conditions [38], [39], [40], [58], [59]. Coupling these methods with operational or real-time forecasting systems, potentially by integrating them into rapid-update cycles, would also be valuable for agricultural stakeholders needing frequent, high-resolution updates on imminent precipitation threats.

Other machine learning approaches beyond GANs can also be employed for tasks of this nature. For example, diffusion models [60], [61], [62] have demonstrated strong potential in synthesizing high-resolution fields, particularly under data-scarce or topographically complex conditions. Exploring these methods alongside cGANs could yield more robust downscaling solutions and further advance high-resolution precipitation modeling. Finally, computational considerations—both in terms of training large U-Net-like networks on extended spatial-temporal domains and running them in real-time operational contexts—should be weighed. Future studies might explore model compression or more advanced GPU parallelization to handle larger volumes of data while maintaining the network's fidelity for small-scale rainfall structures. By iteratively refining these aspects, cGAN-based downscaling stands to become an even more potent tool in climate impact analysis, offering heightened precision and detail where it matters most for critical sectors like agriculture and disaster risk management.

REFERENCES

[1] A. Gershunov, T. Benmarhnia, and R. Aguilera, "Human health implications of extreme precipitation events and water quality in California, USA: A canonical correlation analysis," *Lancet Planet. Health*, vol. 2, p. 9, May 2018.

[2] P. Wang, X. Deng, H. Zhou, and W. Qi, "Responses of urban ecosystem health to precipitation extreme: A case study in Beijing and Tianjin," *J. Cleaner Prod.*, vol. 177, pp. 124–133, Mar. 2018.

[3] Y. Zhao, L. Wang, Q. Jiang, and Z. Wang, "Sensitivity of gross primary production to precipitation and the driving factors in China's agricultural ecosystems," *Sci. Total Environ.*, vol. 948, Oct. 2024, Art. no. 174938.

[4] D. M. Waller, A. G. Meyer, Z. Raff, and S. I. Apfelbaum, "Shifts in precipitation and agricultural intensity increase phosphorus concentrations and loads in an agricultural watershed," *J. Environ. Manage.*, vol. 284, Apr. 2021, Art. no. 112019.

[5] F. Pei, Y. Zhou, and Y. Xia, "Assessing the impacts of extreme precipitation change on vegetation activity," *Agriculture*, vol. 11, no. 6, p. 487, May 2021.

[6] M. S. Abbasian, M. R. Najafi, and A. Abrishamchi, "Increasing risk of meteorological drought in the lake urmia basin under climate change: Introducing the precipitation–temperature deciles index," *J. Hydrol.*, vol. 592, Jan. 2021, Art. no. 125586.

[7] V. Dahal, S. Gautam, and R. Bhattarai, "Analysis of the long-term precipitation trend in Illinois and its implications for agricultural production," *Water*, vol. 10, no. 4, p. 433, Apr. 2018.

[8] G. Sofia, F. Ragazzi, P. Giandon, G. D. Fontana, and P. Tarolli, "On the linkage between runoff generation, land drainage, soil properties, and temporal patterns of precipitation in agricultural floodplains," *Adv. Water Resour.*, vol. 124, pp. 120–138, Feb. 2019.

[9] S. Suryavanshi, N. Joshi, H. K. Maurya, D. Gupta, and K. K. Sharma, "Understanding precipitation characteristics of Afghanistan at provincial scale," *Theor. Appl. Climatol.*, vol. 150, no. 3, pp. 1775–1791, Nov. 2022.

[10] T. Xiang, F. Qiang, G. Liu, C. Liu, Y. Liu, N. Ai, and H. Ma, "Soil quality evaluation of typical vegetation and their response to precipitation in loess hilly and gully areas," *Forests*, vol. 14, no. 9, p. 1909, Sep. 2023.

[11] Y. Zhao, X. Wang, S. Jiang, J. Xiao, J. Li, X. Zhou, H. Liu, Z. Hao, and K. Wang, "Soil development mediates precipitation control on plant productivity and diversity in Alpine grasslands," *Geoderma*, vol. 412, Apr. 2022, Art. no. 115721.

[12] J. G. Arbuckle, L. W. Morton, and J. Hobbs, "Understanding farmer perspectives on climate change adaptation and mitigation: The roles of trust in sources of climate information, climate change beliefs, and perceived risk," *Environ. Behav.*, vol. 47, no. 2, pp. 205–234, Feb. 2015.

[13] M. T. Niles, M. Brown, and R. Dynes, "Farmer's intended and actual adoption of climate change mitigation and adaptation strategies," *Climatic Change*, vol. 135, no. 2, pp. 277–295, Mar. 2016.

[14] R. Sharma, A. Shishodia, S. Kamble, A. Gunasekaran, and A. Belhadi, "Agriculture supply chain risks and COVID-19: Mitigation strategies and implications for the practitioners," *Int. J. LogisticsRes. Appl.*, vol. 27, no. 11, pp. 2351–2377, Nov. 2024.

[15] L. C. Stringer, E. D. G. Fraser, D. Harris, C. Lyon, L. Pereira, C. F. M. Ward, and E. Simelton, "Adaptation and development pathways for different types of farmers," *Environ. Sci. Policy*, vol. 104, pp. 174–189, Feb. 2020.

[16] J. E. Kay et al., "The community Earth system model (CESM) large ensemble project: A community resource for studying climate change in the presence of internal climate variability," *Bull. Amer. Meteorolog. Soc.*, vol. 96, no. 8, pp. 1333–1349, Aug. 2015.

[17] N. Maher et al., "The max Planck institute grand ensemble: Enabling the exploration of climate system variability," *J. Adv. Model. Earth Syst.*, vol. 11, no. 7, pp. 2050–2069, Jul. 2019.

[18] N. C. Swart et al., "The Canadian earth system model version 5 (CanESM5. 0.3)," *Geosci. Model Develop.*, vol. 12, no. 11, pp. 4823–4873, 2019.

[19] S.-T. Chen, P.-S. Yu, and Y.-H. Tang, "Statistical downscaling of daily precipitation using support vector machines and multivariate analysis," *J. Hydrol.*, vol. 385, nos. 1–4, pp. 13–22, May 2010.

[20] J. Schmidli, C. Frei, and P. L. Vidale, "Downscaling from GCM precipitation: A benchmark for dynamical and statistical downscaling methods," *Int. J. Climatol. A J. Roy. Meteorolog. Soc.*, vol. 26, no. 5, pp. 679–689, 2006.

[21] S. P. Charles, B. C. Bates, I. N. Smith, and J. P. Hughes, "Statistical downscaling of daily precipitation from observed and modelled atmospheric fields," *Hydrolog. Processes*, vol. 18, no. 8, pp. 1373–1394, Jun. 2004.

[22] J. Huang, J. Zhang, Z. Zhang, C. Xu, B. Wang, and J. Yao, "Estimation of future precipitation change in the Yangtze river basin by using statistical downscaling method," *Stochastic Environ. Res. Risk Assessment*, vol. 25, no. 6, pp. 781–792, Aug. 2011.

[23] S. Cao, C. Cao, Y. Li, and L. Zhu, "A statistical downscaling model based on multiway functional principal component analysis for southern Australia winter rainfall," *J. Appl. Meteorol. Climatol.*, vol. 62, no. 6, pp. 677–689, Jun. 2023.

[24] F. Wetterhall, A. Bárdossy, D. Chen, S. Halldin, and C. Xu, "Daily precipitation-downscaling techniques in three Chinese regions," *Water Resour. Res.*, vol. 42, no. 11, pp. 1–13, Nov. 2006.

[25] T. Lafon, S. Dadson, G. Buys, and C. Prudhomme, "Bias correction of daily precipitation simulated by a regional climate model: A comparison of methods," *Int. J. Climatol.*, vol. 33, no. 6, pp. 1367–1381, May 2013.

[26] M. Mendez, B. Maathuis, D. Hein-Griggs, and L.-F. Alvarado-Gamboa, "Performance evaluation of bias correction methods for climate change monthly precipitation projections over Costa Rica," *Water*, vol. 12, no. 2, p. 482, Feb. 2020.

[27] L. Guo, Z. Jiang, D. Chen, H. L. Treut, and L. Li, "Projected precipitation changes over China for global warming levels at 1.5 °C and 2 °C in an ensemble of regional climate simulations: Impact of bias correction methods," *Climatic Change*, vol. 162, no. 2, pp. 623–643, Aug. 2020.

[28] Y. Yang, J. Tang, Z. Xiong, S. Wang, and J. Yuan, "An intercomparison of multiple statistical downscaling methods for daily precipitation and temperature over China: Present climate evaluations," *Climate Dyn.*, vol. 53, nos. 7–8, pp. 4629–4649, Oct. 2019.

[29] S. Tripathi, V. V. Srinivas, and R. S. Nanjundiah, "Downscaling of precipitation for climate change scenarios: A support vector machine approach," *J. Hydrol.*, vol. 330, nos. 3–4, pp. 621–640, Nov. 2006.

[30] X. He, N. W. Chaney, M. Schleiss, and J. Sheffield, "Spatial downscaling of precipitation using adaptable random forests," *Water Resour. Res.*, vol. 52, no. 10, pp. 8217–8237, Oct. 2016.

[31] J. Zhang, H. Fan, D. He, and J. Chen, "Integrating precipitation zoning with random forest regression for the spatial downscaling of satellite-based precipitation: A case study of the Lancang–Mekong river basin," *Int. J. Climatol.*, vol. 39, no. 10, pp. 3947–3961, Aug. 2019.

[32] T. Tu, K. Ishida, A. Ercan, M. Kiyama, M. Amagasaki, and T. Zhao, "Hybrid precipitation downscaling over coastal watersheds in Japan using WRF and CNN," *J. Hydrol., Regional Stud.*, vol. 37, Oct. 2021, Art. no. 100921.

[33] J. Kim, M. Lee, H. Han, D. Kim, Y. Bae, and H. S. Kim, "Case study: Development of the CNN model considering teleconnection for spatial downscaling of precipitation in a climate change scenario," *Sustainability*, vol. 14, no. 8, p. 4719, Apr. 2022.

[34] T. G. Asfaw and J.-J. Luo, "Downscaling seasonal precipitation forecasts over east Africa with deep convolutional neural networks," *Adv. Atmos. Sci.*, vol. 41, no. 3, pp. 449–464, Mar. 2024.

[35] D. Tran Anh, S. P. Van, T. D. Dang, and L. P. Hoang, "Downscaling rainfall using deep learning long short-term memory and feedforward neural network," *Int. J. Climatol.*, vol. 39, no. 10, pp. 4170–4188, Aug. 2019.

[36] N. C. Fouotsa Manfouo, L. Potgieter, A. Watson, and J. H. Nel, "A comparison of the statistical downscaling and long-short-term-memory artificial neural network models for long-term temperature and precipitations forecasting," *Atmosphere*, vol. 14, no. 4, p. 708, Apr. 2023.

[37] B. Kumar, K. Atey, B. B. Singh, R. Chattopadhyay, N. Acharya, M. Singh, R. S. Nanjundiah, and S. A. Rao, "On the modern deep learning approaches for precipitation downscaling," *Earth Sci. Informat.*, vol. 16, no. 2, pp. 1459–1472, Jun. 2023.

[38] L. Harris, A. T. T. McRae, M. Chantry, P. D. Dueben, and T. N. Palmer, "A generative deep learning approach to stochastic downscaling of precipitation forecasts," *J. Adv. Model. Earth Syst.*, vol. 14, no. 10, p. 2022, Oct. 2022.

[39] L. Glawion, J. Polz, H. Kunstmann, B. Fersch, and C. Chwala, "spateGAN: Spatio-temporal downscaling of rainfall fields using a cGAN approach," *Earth Space Sci.*, vol. 10, no. 10, 2023, Art. no. e2023EA002906.

[40] N. Rampal, P. B. Gibson, S. Sherwood, G. Abramowitz, and S. Hobeichi, "A reliable generative adversarial network approach for climate downscaling and weather generation," *J. Adv. Model. Earth Syst.*, vol. 17, no. 1, p. 2024, Jan. 2025.

[41] N. Hayatbini, B. Kong, K.-L. Hsu, P. Nguyen, S. Sorooshian, G. Stephens, C. Fowlkes, R. Nemani, and S. Ganguly, "Conditional generative adversarial networks (cGANs) for near real-time precipitation estimation from multispectral GOES-16 satellite imageries—PERSIANN-cGAN," *Remote Sens.*, vol. 11, no. 19, p. 2193, Sep. 2019.

[42] E. Becker, P. Pandit, S. Rangan, and A. K. Fletcher, "Instability and local minima in GAN training with kernel discriminators," in *Proc. Adv. Neural Inf. Process. Syst.*, vol. 35, Jan. 2022, pp. 20300–20312.

[43] M. Welfert, G. R. Kurri, K. Otstot, and L. Sankar, "Addressing GAN training instabilities via tunable classification losses," *IEEE J. Sel. Areas Inf. Theory*, vol. 5, pp. 534–553, 2024.

[44] I. Gulrajani, F. Ahmed, M. Arjovsky, V. Dumoulin, and A. Courville, "Improved training of Wasserstein GANs," in *Proc. Adv. Neural Inf. Process. Syst.*, vol. 30, Dec. 2017, pp. 5769–5779.

[45] M. Zheng, T. Li, R. Zhu, Y. Tang, M. Tang, L. Lin, and Z. Ma, "Conditional Wasserstein generative adversarial network-gradient penalty-based approach to alleviating imbalanced data classification," *Inf. Sci.*, vol. 512, pp. 1009–1023, Feb. 2020.

[46] J. Zhang, K. Howard, C. Langston, B. Kaney, Y. Qi, L. Tang, H. Grams, Y. Wang, S. Cocks, S. Martinaitis, A. Arthur, K. Cooper, J. Brogden, and D. Kitzmiller, "Multi-radar multi-sensor (MRMS) quantitative precipitation estimation: Initial operating capabilities," *Bull. Amer. Meteorolog. Soc.*, vol. 97, no. 4, pp. 621–638, Apr. 2016.

[47] H. Habibi, R. Awal, A. Fares, and M. Temimi, "Performance of multi-radar multi-sensor (MRMS) product in monitoring precipitation under extreme events in Harris county, Texas," *J. Hydrol.*, vol. 598, Jul. 2021, Art. no. 126385.

[48] S. Moazami and M. R. Najafi, "A comprehensive evaluation of GPM-IMERG V06 and MRMS with hourly ground-based precipitation observations across Canada," *J. Hydrol.*, vol. 594, Mar. 2021, Art. no. 125929.

[49] J. L. Bytheway, M. R. Abel, K. Mahoney, and R. Cifelli, "A multi-scale evaluation of multisensor quantitative precipitation estimates in the Russian river basin," *J. Hydrometeorol.*, vol. 20, no. 3, pp. 447–466, Mar. 2019.

[50] W. Lei, H. Qin, X. Hou, and H. Chen, "A two-stage model for spatial downscaling of daily precipitation data," *Vis. Comput.*, vol. 40, no. 11, pp. 8263–8286, Nov. 2024.

[51] J. Wang, Z. Liu, I. Foster, W. Chang, R. Kettimuthu, and V. R. Kotamarthi, "Fast and accurate learned multiresolution dynamical downscaling for precipitation," *Geosci. Model Develop.*, vol. 14, no. 10, pp. 6355–6372, Oct. 2021.

[52] T. Vandal, E. Kodra, S. Ganguly, A. Michaelis, R. Nemani, and A. R. Ganguly, "DeepSD: Generating high resolution climate change projections through single image super-resolution," in *Proc. 23rd ACM SIGKDD Int. Conf. Knowl. Discovery Data Mining*, Aug. 2017, pp. 1663–1672.

[53] I. Goodfellow, J. Pouget-Abadie, M. Mirza, B. Xu, D. Warde-Farley, S. Ozair, A. Courville, and Y. Bengio, "Generative adversarial networks," *Commun. ACM*, vol. 63, no. 11, pp. 139–144, Oct. 2020.

[54] I. Goodfellow, J. Pouget-Abadie, M. Mirza, B. Xu, D. Warde-Farley, S. Ozair, A. Courville, and Y. Bengio, "Generative adversarial nets," in *Proc. Adv. Neural Inf. Process. Syst.*, vol. 27, 2014, pp. 1–9.

[55] M. A. Talab, S. Awang, and S. A. M. Najim, "Super-low resolution face recognition using integrated efficient sub-pixel convolutional neural network (ESPCN) and convolutional neural network (CNN)," in *Proc. IEEE Int. Conf. Autom. Control Intell. Syst. (I2CACIS)*, Jun. 2019, pp. 331–335.

[56] X. Zheng, H. Qin, W. Wang, W. Lei, and P. Shi, "Research on precipitation nowcasting based on spatiotemporal cooperative attention," *J. Earth Syst. Sci.*, vol. 134, no. 1, p. 48, Feb. 2025.

[57] F. Yang, Q. Ye, K. Wang, and L. Sun, "Successful precipitation downscaling through an innovative transformer-based model," *Remote Sens.*, vol. 16, no. 22, p. 4292, Nov. 2024.

[58] A. Saha and S. Ravela, "Statistical-physical adversarial learning from data and models for downscaling rainfall extremes," *J. Adv. Model. Earth Syst.*, vol. 16, no. 6, p. 2023, Jun. 2024.

[59] J. Leinonen, D. Nerini, and A. Berne, "Stochastic super-resolution for downscaling time-evolving atmospheric fields with a generative adversarial network," *IEEE Trans. Geosci. Remote Sens.*, vol. 59, no. 9, pp. 7211–7223, Sep. 2021.

[60] F. Ling, Z. Lu, J.-J. Luo, L. Bai, S. K. Behera, D. Jin, B. Pan, H. Jiang, and T. Yamagata, "Diffusion model-based probabilistic downscaling for 180-year east Asian climate reconstruction," *npj Climate Atmos. Sci.*, vol. 7, no. 1, p. 131, Jun. 2024.

[61] Z. Gao, X. Shi, B. Han, H. Wang, X. Jin, D. C. Maddix, Y. Zhu, M. Li, and Y. Wang, "PreDiff: Precipitation nowcasting with latent diffusion models," in *Proc. Adv. Neural Inf. Process. Syst.*, vol. 36, Jan. 2023, pp. 78621–78656.

[62] C. Nai, B. Pan, X. Chen, Q. Tang, G. Ni, Q. Duan, B. Lu, Z. Xiao, and X. Liu, "Reliable precipitation nowcasting using probabilistic diffusion models," *Environ. Res. Lett.*, vol. 19, no. 3, Mar. 2024, Art. no. 034039.

JANGHO LEE received the B.S. degree in earth and environmental sciences from Seoul National University, Seoul, South Korea, in 2018, and the Ph.D. degree in atmospheric sciences from Texas A&M University, College Station, TX, USA, in 2023.

Since 2023, he has been a Postdoctoral Researcher with the University of Illinois at Chicago, as a part of the Community Research on Climate and Urban Science (CROCUS) Project. His research interests include climate informatics, statistical climatology, deep learning, remote sensing, climate impacts, and land-atmospheric modeling.

Dr. Lee has been a member of American Geophysical Union (AGU) and American Meteorological Society (AMS), since 2018.

SUN YOUNG PARK received the B.S. and M.S. degrees in civil and environmental engineering from Seoul National University, Seoul, South Korea, in 2009 and 2013, respectively. She is currently pursuing the Ph.D. degree in civil and environmental engineering with the University of Illinois at Urbana–Champaign, Urbana, IL, USA, focusing on computational hydraulics and hydrology.

She has been working on the Community Research on Climate and Urban Science (CROCUS) Project, since 2023. She has contributed to understanding the Chicago area waterway system (CAWS) under high-impact weather and regional precipitation systems. Her research interests include urban meteorology, hydrology, hydraulics, integrating modeling, and observations. Her expertise includes deep learning applications, storm water modeling, and mesoscale meteorology.

Ms. Park is a member of American Geophysical Union (AGU) and American Meteorological Society (AMS) and actively participates in professional organizations related to hydrology and climate science.